Dalton Transactions

ROYAL SOCIETY OF CHEMISTRY

PAPER

View Article Online
View Journal | View Issue

Cite this: *Dalton Trans.*, 2025, **54**, 10097

Dicopper(II) metallacyclophanes featuring acridine-based spacers: long-range magnetic coupling and selective catalytic oxidation of hydroquinone†‡

Lucas Hoffmann Greghi Kalinke, [a] Maria Clara Orioli Emidio Souza, [b] Pedro Victor Valadares Romanholo, [b] Jackson Junior Santos de Souza, [b] Antonio Carlos Roveda, Jr., [c] Sergio Antonio Spinola Machado, [c] Ana Karoline Silva Mendanha Valdo, [d] Felipe Terra Martins, [b] Renato Rabelo, [b,e] Joan Cano, *[e] Francesc Lloret, [e] Miguel Julve, [e] Livia Flório Sgobbi *[b] and Danielle Cangussu *[b]

Received 2nd May 2025,
Accepted 2nd June 2025

DOI: 10.1039/d5dt01037c

rsc.li/dalton

The copper(II) complexes $\{Na_4(H_2O)_8[Cu_2(acriba)_2(H_2O)_2]\}_n \cdot 4nH_2O$ (**1**) and $(Bu_4N)_4[Cu_2(acriba)_2]\cdot 5H_2O$ (**2**) [H_4acriba = *N*,*N*′-3,6-acridinebis(oxamic acid) and Bu_4N^+ = tetra-*n*-butylammonium cation] have been synthesized and characterized. Their crystal structures revealed the occurrence of $[Cu_2(acriba)_2(H_2O)_2]^{4-}$ (**1**) and $[Cu_2(acriba)_2]^{4-}$ (**2**) units of the [3,3] metallacyclophane-type which are built by two acridine linkers connected by two N–Cu–N bonds. The electroneutrality in **1** is achieved by their coordination to hydrated sodium(I) cations to afford a heterobimetallic sheet-like polymer, whereas that in **2** is ensured by bulky organic Bu_4N^+ cations to yield well-separated discrete dicopper(II) complexes. The spectrophotometric study of the catalytic activity of **1** and the related complex $[Na_6Cu_2(mpyba)_2Cl_2(H_2O)_8]\cdot 7H_2O$ (**3**) [H_4mpyba = *N*,*N*′-2,6-pyridinebis(oxamic acid)] towards the oxidation of phenolic derivatives in aqueous solution showed a remarkable catalytic performance only for the hydroquinone with a better catalytic role in the case of **1**. This superior catalytic behavior may be explained by the higher Lewis acidity of the Cu(II) ions derived from the inherent electronic delocalization of the extended aromatic acridine fragment compared to the pyridine one. The magnetic properties of **1** and **2** show weak intramolecular ferromagnetic interactions within their metallacyclophane units [J = +1.83 (**1**) and +1.72 cm^{-1} (**2**); $\boldsymbol{H} = -J\boldsymbol{S}_{Cu1}\cdot\boldsymbol{S}_{Cu2}$ where $S_{Cu1} = S_{Cu2} = 1/2$], their nature and magnitude being substantiated by theoretical calculations. These two examples illustrate the ability of the acridine moieties to mediate ferromagnetic interactions between copper(II) ions through the very long $-N_{amidate}-C-C-C-N-C-C-C-N_{amidate}-$ exchange pathway in the context of the spin polarization mechanism.

Introduction

Copper-based enzymes and proteins comprise an important class of biologically active compounds. The coordination of copper within the protein structure plays a pivotal role in its biochemical activity. For instance, many copper-containing enzymes work in dioxygen binding, activation and further substrate oxidation, as performed by monooxygenases, dioxygenases and oxidases.[1] Among them, multicopper oxidases (MCOs) are appealing catalysts in a wide range of biotechnological applications, especially bioremediation and biosensing.[2] Despite the versatility displayed by MCOs, their activity is limited by intrinsic vulnerabilities, involving low thermal stability and restricted environment tolerance (pH and non-aqueous solvents).[3] Additionally, the high cost associated with

[a]*Instituto Federal de Goiás, Campus Anápolis, Anápolis, Goiás, 75131-457, Brazil*
[b]*Instituto de Química, Universidade Federal de Goiás, Goiânia, Goiás, 74690-900, Brazil. E-mail: danielle_cangussu@ufg.br, livia_sgobbi@ufg.br*
[c]*Instituto de Química de São Carlos, Universidade de São Paulo, São Carlos, São Paulo, 13566-590, Brazil*
[d]*Instituto Federal Goiano, Campus Iporá, Iporá, Goiás, 74200-264, Brazil*
[e]*Departament de Química Inorgànica/Instituto de Ciencia Molecular (ICMol), C/ Catedrático José Beltrán 2, 46980 Paterna, Valencia, Spain. E-mail: joan.cano@uv.es*

† In loving memory of Miguel Julve, our dear friend and colleague, whose legacy as a professor and researcher will continue to inspire us all.

‡ Electronic supplementary information (ESI) available. CCDC 2083644 and 2207096. For ESI and crystallographic data in CIF or other electronic format see DOI: https://doi.org/10.1039/d5dt01037c

laborious extraction and purification processes hinders the use of natural enzymes in industrial and commercial applications.[4] Another critical issue is their selectivity since some enzymes recognize a broad spectrum of substrates. Laccases, one of the major MCO superfamilies, act on phenolic substrates by catalysing the oxidation of phenolic hydroxyl groups to phenoxy radicals, reducing dioxygen to water.[5] Their substrate spectrum includes mono-, di-, and polyphenols, methoxy-substituted phenols, aromatic compounds, and amines.[6] The poor selectivity restrains their use in biosensing approaches due to the inability to distinguish a target analyte from other species in a complex matrix.[7] Thereby, the development of artificial enzymes that can be finely designed to mimic the structure or functions of natural enzymes is highly appealing.[8] In this respect, metallobiosites have attracted considerable research efforts in the last few decades, encompassing the interest in understanding their structures and mechanisms and the search to mimic their catalytic activities.[9]

Metallosupramolecular systems also offer a microenvironment resembling an enzymatic active site, containing selective binding moieties and non-covalent interactions to promote reactivity and selectivity not observed in bulk solution.[10] The multimetallic enzymatic centers are not only the most challenging to mimic, but also very attractive due to their role in activating small molecules.[11] In particular, the chemistry of the aromatic-substituted oligooxamate ligands is a prominent approach to design multimetallic coordination architectures.[12] These multifunctional metallosupramolecular structures with practically infinite possibilities of chemical functionalization, exhibit appealing properties, such as high stability of oxamate-containing copper(II) complexes in solution,[13] slow relaxation of the magnetization,[14] chiral single chain magnet behavior,[15] therapeutic uses,[16] gas and vapor sorption,[17] potential magnetic molecular wires[18] and cheap and environmentally benign catalysts[19] among others.

Herein, we report the synthesis and magneto-structural investigation of two new compounds of formulas $\{Na_4(H_2O)_8[Cu_2(acriba)_2(H_2O)_2]\}_n{\cdot}4nH_2O$ (**1**) and $(Bu_4N)_4[Cu_2(acriba)_2]{\cdot}5H_2O$ (**2**) [H_4acriba = *N*,*N*′-3,6-acridinebis (oxamic acid) and Bu_4N^+ = tetra-*n*-butylammonium cation] (see Scheme 1) together with a study of the catalytic properties of **1** and its related parent complex $[Na_6Cu_2(mpyba)_2Cl_2(H_2O)_8]{\cdot}7H_2O$ (**3**) [H_4mpyba = *N*,*N*′-2,6-pyridinebis(oxamic acid)][12a] towards the aerobic oxidation of resorcinol, catechol and hydroquinone. Also, a detailed study of the magnetic properties of **1** and **2**, supported by theoretical calculations, provides more insights into the spin delocalisation mechanism.

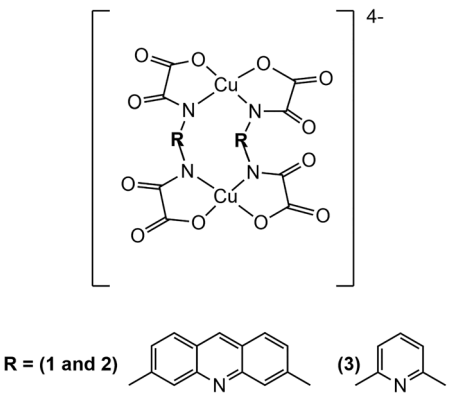

Scheme 1 Structural formula of the [3,3] metallacycophane-type skeleton in **1–3**.

Results and discussion

Synthesis, powder X-ray diffraction, infrared and electronic spectra

The preparation of the Et_2H_2acriba proligand follows that previously reported for similar species.[20] Compound **1** was obtained as polycrystalline powder in a good yield by the reaction of copper(II) nitrate trihydrate and Et_2H_2acriba after deprotonation and hydrolysis with NaOH [1 : 1 : 4 Cu(II) : proligand : base molar ratio] in water by using ethanol as the precipitating agent. Green needle-like crystals of **1** were grown in a test tube by slow diffusion of acetonitrile into an aqueous solution of a powder sample of **1**. A similar procedure was used to isolate **2** from its aqueous solution, using Bu_4NOH and $CuClO_4{\cdot}6H_2O$ as the base and source of copper(II). Recrystallization in acetone of the solid obtained afforded X-ray quality crystals of **2**, which are highly hygroscopic. The powder X-ray diffraction patterns of bulk sample of **1** confirm their phase purity (Fig. S1, ESI‡).

FT-IR spectra of Et_2H_2acriba, **1** and **2** are shown in Fig. S2.‡ The most prominent peaks in the infrared spectrum of the proligand are a medium absorption at 3337 cm^{-1}, which is due to N–H stretching vibration of the amide fragment, and two strong absorptions at 1730 and 1624 cm^{-1} corresponding to carbonyl stretchings of the acid ester groups. The shift of these strong absorptions to lower wavelengths in the infrared spectra of both **1** and **2** (1638 and 1592 cm^{-1}) as well as the lack of the amide N–H stretching suggests the coordination of the copper(II) ions to the deprotonated amide nitrogen and carboxylate oxygen atoms in **1** and **2**. The multiple absorptions in the range 2930–2870 cm^{-1} in the case of **2** are due to the C–H stretching of the tetra-*n*-butylammonium cation. Finally, the strong and broad absorption centered at 3400 cm^{-1} on the spectra of **1** and **2** is due to the presence of water molecules.

The electronic spectra of a solid sample of **1** exhibit a broad band centred at 670 nm corresponding to d–d transitions of square pyramidal copper(II) ions (Fig. S3‡).[13b] The high hygroscopicity prevails in recording the electronic spectra of **2** in the solid-state. The electronic spectra of **1** and **2** in aqueous solution exhibit practically identical very intense absorption bands at 241 nm (41 493 cm^{-1}) and 276 nm (36 231 cm^{-1}) attributed to π–π* intraligand transitions as well as another one at 386 nm (25 907 cm^{-1}) which is due to a metal-to-ligand charge transfer (MLCT) transition which precludes the observation of the d–d transition bands (Fig. S4‡).

Structural descriptions of 1 and 2

Compound **1** crystallizes in the non-centrosymmetric $P2_1$ space group with two fully deprotonated acridine-oxamate ligands, two copper(II) and four sodium(I) cations, ten coordinated and four non-coordinated water molecules in the asymmetric unit. Compound **2** was solved in the centrosymmetric triclinic $P\bar{1}$ space group with two fully deprotonated acridine-oxamate ligands, two copper(II) ions and four tetrabutylammonium cations plus five water molecules of crystallization in the asymmetric unit. Each acriba^{4-} ligand in **1** and **2** is coordinated to the two crystallographically independent copper(II) ions through its oxamate groups by the deprotonated amide-nitrogen and one carboxylate-oxygen atom resulting in a 20-membered metallaaza-linked [3,3] metallacyclophane ring system (Fig. 1a and 2a). Since the aforementioned metallacyclophane ring is common in **1** and **2** (root-mean-square deviation for the common superimposed atoms being equal to 0.374 Å; Fig. 2b), except for the copper-coordinated water molecules in the apical positions present only in **1**, hereinafter we will mainly focus on the first compound to describe its backbone. The two crystallographically independent acriba^{4-} ligands are stacked face-to-face, establishing π···π interactions featured by an angle of 5.7(2)° between the least-squares planes calculated through the acridine non-hydrogen atoms. The centroids calculated through the atoms of the π-stacked side rings are spaced by 3.506(4) and 3.551(4) Å with corresponding slippages of 0.871 and 0.404 Å, while this distance and the offset one are 3.592(4) and 0.591 Å for the atoms of the central pyridine ring. Additionally, to the four basal atoms from the two stacked acriba^{4-} ligands, each copper(II) ion in **1** is also coordinated by one water molecule in the apical position leading to a somewhat distorted square pyramidal surrounding [the values of the trigonality parameter (τ) being 0.07 and 0.15 for Cu1 and Cu2, respectively].[21] Interestingly, these apical water molecules point towards opposite sides of the respective mean basal planes.

The root-mean square deviation for the N3N6O6O12 set of atoms at Cu1 is 0.193 Å, with the greatest deviation of 0.201 (15) Å for O12, while that parameter is 0.334 Å for N1N4O3O9

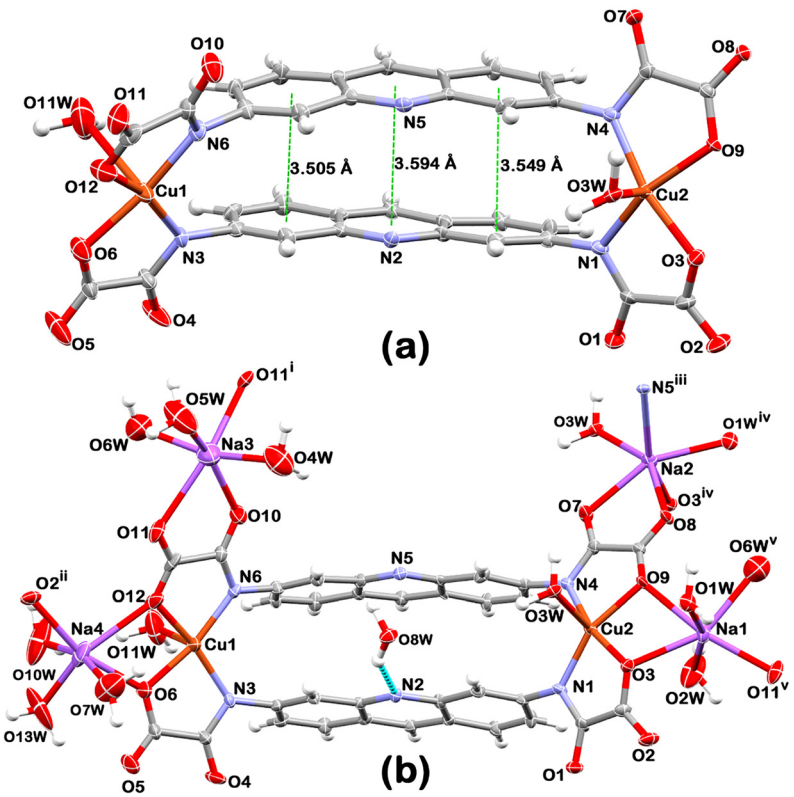

Fig. 1 (a) A perspective view of the [3,3] metallacyclophane-type dicopper(II) fragment in **1**. Here and in the next picture, green dashed lines denote the π···π interactions (the displayed distances were measured between the centroids calculated through each one of the three six-ring atoms of the acridine moiety). (b) A view of the dicopper(II) metallacyclophane's assembling role towards the sodium ions shows the coordination environment of the four crystallographically independent alkaline cations. Cyan dashed line outlines the hydrogen bond between one water molecule of crystallization and the acridine-nitrogen atom here and in the next picture. O13W and O14W belong to the same disordered water molecule and are in 60 and 40% occupancy sites, respectively, but O14 and its hydrogen atoms were omitted for clarity in this panel. In both panels and in panel (a) of the next picture, all non-hydrogen atoms were drawn at the 30% probability level, whereas the hydrogen atoms are represented with spheres of arbitrary radius. Carbon and hydrogen atoms were not labelled [Symmetry code: (i) = $-x, \frac{1}{2}+y, 1-z$; (ii) = $x, y, -1+z$; (iii) = $-x, \frac{1}{2}+y, 2-z$; (iv) = $x, 1+y, z$; (v) = $x, y, 1+z$].

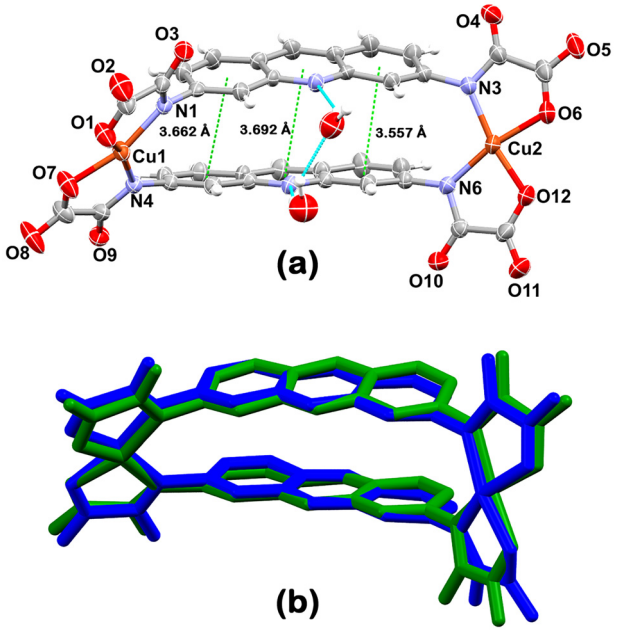

Fig. 2 (a) A perspective view of the [3,3] metallacyclophane-type dicopper(II) complex in **2**. (b) A molecular overlay between the [3,3] metallacyclophane-type dicopper(II) moieties in **1** (blue) and **2** (green). Hydrogen atoms and copper-coordinated water molecules present only in **1** (O3W and O11W labelled in Fig. 1) were omitted in the superimposition calculation.

at Cu2, with the greatest deviation of 0.396(14) Å for N1. Notably, the basal plane at Cu2 is more distorted than at Cu1. Furthermore, the basal planes of the two crystallographically independent copper atoms exhibit different bents relative to the acridine mean planes. The basal plane at Cu1 forms angles of 62.6(3) and 66.1(3)° with the acridine ones bearing the N2 and N5 atoms, respectively, while they are 86.7(3) and 81.1(3)° for the basal plane at Cu2. The intramolecular Cu1···Cu2 separation within the dicopper(II) unit is 11.477(4) Å. This value is greater than the shorter intramolecular copper–copper separation between the metallacyclophane units through the sodium(I) ions in 1 [7.524(3) Å for Cu2···Cu2^{iv}]. These values compare well with those in **2** [11.535(2) and 8.283(2) Å for Cu1···Cu2 and Cu2···Cu2^{vi}, respectively; (vi): $1-x$, $1-y$, $1-z$].

The two crystallographically independent acriba^{4-} ligands differ in their binding pattern to the sodium ions (Fig. 1b and S5‡). So, whereas both acriba^{4-} ligands engage their oxamate oxygen atoms (already coordinated to the copper(II) ions) in the binding to the Na1 and Na4 sodium centres at the flanks of the dicopper(II) [3,3] metallacyclophane unit, connecting them horizontally along the crystallographic *c* axis (Fig. S5‡), only one acriba^{4-} ligand (that containing the N5 atom) is coordinated to Na2 and Na3 through its four oxygen atoms from the two oxamate moieties which are not coordinated to the copper centres. Such bifurcated binding patterns are responsible for connecting vertically the dicopper(II) fragments along the crystallographic *b* axis in a ladder-like fashion (Fig. S5,‡ bottom). Only one oxygen atom (O2) from the acriba^{4-} ligand bearing the N2 atom is bonded to a sodium ion (Na4). All four crystallographically sodium ions are six-coordinated in trigonal antiprism environments with oxamate-oxygen and water molecules as main donors. Only one acridine nitrogen atom (N5) is interacting with a sodium ion (Na2) (Fig. S6‡), which also connects the dicopper(II) units along the crystallographic *c* axis together with Na3–O10 and Na3–O11 bonds, completing an imbricate coordination layer distributed over the (100) plane (Fig. S6‡). Hydrogen bonds involving water molecules and oxamate groups connect these sheets along an axis (see Table S4‡), featuring a supramolecular 3D coordination polymer (Fig. S6‡). Remarkably, the acridine nitrogen (N_2) is a hydrogen bonding acceptor from one water molecule of crystallization (O8W–H8A) (Fig. 1b). Water–acridine hydrogen bonds are also present in **2** (Fig. 2a and S7‡), leading to an imbricated hydrogen bonding network involving water molecules of crystallization and oxamate-oxygen atoms. Together with the weaker interactions from the tetrabutylammonium cations, these hydrogen bonds are responsible for the crystal packing (see Table S5‡ for the hydrogen bonds metrics in **2**).

Kinetic activity of 1 and 3 towards the hydroquinone oxidation

The catalytic activities of complexes **1** and **3** were evaluated spectrophotometrically in the presence of phenolic compounds. For this purpose, *ortho*-, *meta*- and *para*-substituted phenolic compounds, catechol, resorcinol and hydroquinone (H_2Q), were selected. Both complexes exhibited significant catalytic activity exclusively toward H_2Q (Fig. 3, S9 and S10‡). The spontaneous oxidation of H_2Q by the atmospheric molecular oxygen, in the absence of a catalyst, proceeds slowly, resulting in negligible changes in the UV-Vis spectra even after one hour (Fig. S8‡). In contrast, in the presence of either **1** or **3**, the development of an absorption band at 245 nm, characteristic of *p*-benzoquinone (BQ) formation (an oxidation product of H_2Q),[22] was observed over time (Fig. 3).

To evaluate the interaction of H_2Q with complexes **1** and **3**, the initial rates of absorbance increase at 245 nm were measured for various H_2Q concentrations while maintaining a constant catalyst concentration (15 μmol L^{-1}). The resulting double-logarithmic plots (Fig. 4) support pseudo first-order kinetics, with reaction orders (n) close to 1 and apparent first-order rate constants (k_{obs}) of 5.35 for **1** and 1.04 s^{-1} for **3**.

The superior catalytic performance of **1** compared to **3** is likely attributed to the enhanced π-conjugation of the acridine spacer, which facilitates electron delocalization across the ligand framework. This delocalization increases the Lewis acidity of the Cu(II) center, promoting dioxygen activation and substrate coordination. The greater Lewis acidity in **1** enhances the Cu center's ability to accept electrons, which in turn promotes the oxidation of hydroquinone. Moreover, this increased acidity modulates the electronic structure of both ligand environment and the metal center, contributing to the overall catalytic performance of the complex.[22]

The oxidation of H_2Q to BQ is a well-known model reaction used to assess the performance of various copper-based cata-

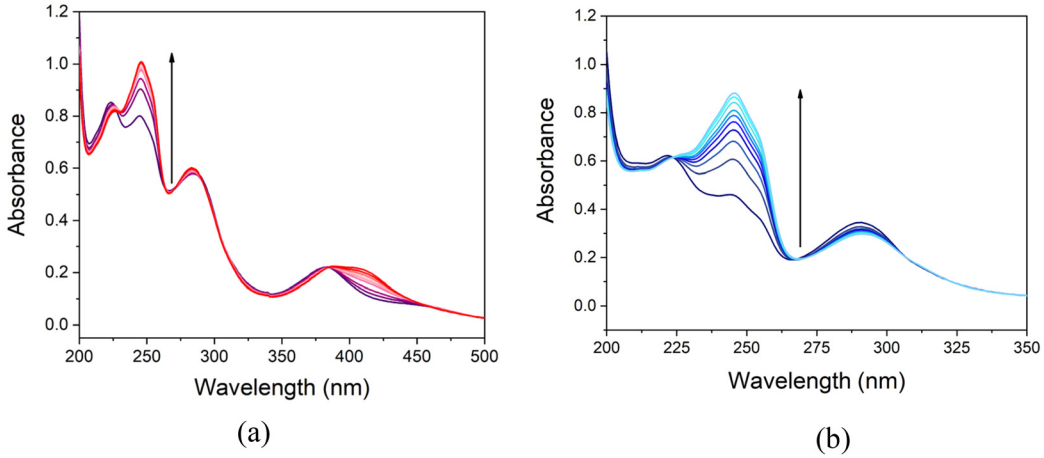

Fig. 3 Evolution of the electronic absorption spectra of the oxidation of H_2Q into BQ (λ_{max} = 245 nm) catalysed by **1** (a) and **3** (b) at 25 °C under dioxygen saturation. The arrows indicate the course of the reaction during one hour. $[H_2Q]_0$ = 75 μmol L^{-1} and [**1**] = [**3**] = 7.5 μmol L^{-1}.

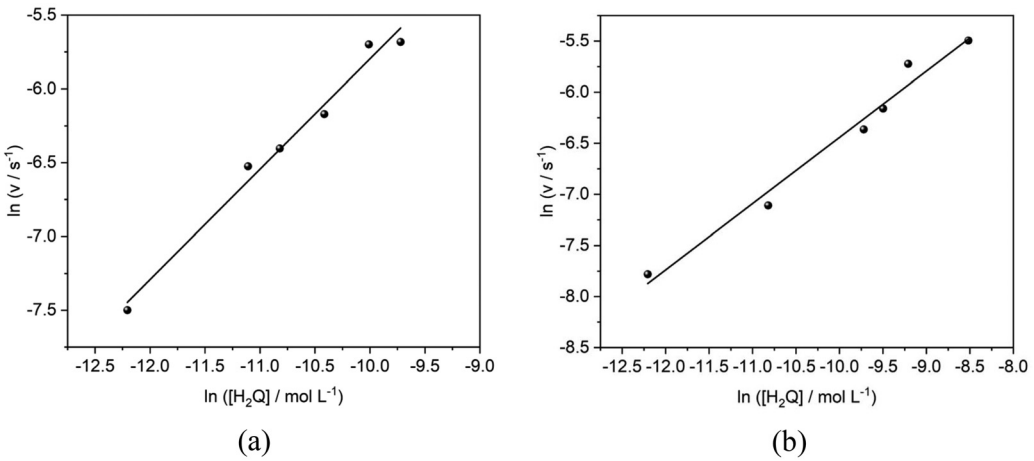

Fig. 4 Double-logarithmic plot of ln ν *versus* ln [H_2Q] for **1** (a) and **3** (b). The concentrations of **1** and **3** were fixed at 15 μmol L^{-1} while that of H_2Q ranged from 5 to 200 μmol L^{-1}.

lysts. Although this reaction proceeds slowly at room temperature in the absence of a catalyst, it is significantly accelerated in the presence of Cu(II) centers and oxidizing agents such as molecular oxygen or hydrogen peroxide. When concentrated hydrogen peroxide solutions are used, further oxidation of the reaction product BQ to 2,5-dihydroxy-*p*-benzoquinone may occur. However, the use of H_2O_2 is impractical for the development of sensing devices, since it requires the addition of an external reactant.

Several studies have investigated Cu(II)-based complexes as catalysts for H_2Q oxidation, typically employing hydrogen peroxide as the oxidant. For instance, the polymer-anchored complex [Cu(saldien)] (H_2saldien = *N*,*N*′-bis(salicylidene)diethylenetriamine) was studies as a catalyst for HQ oxidation using high concentration of H_2O_2 (30%) at pH 10.[23] Similarly, copper sorbed on chitosan flakes copper immobilized on chitosan flakes showed higher transformation rates with H_2O_2 than with air, though at the cost of reduced selectivity.[24] Cu(II) ions immobilized on acrylic resins with aminoguanidyl ligands also exhibited catalytic activity in aqueous media, again relying on high H_2O_2 concentrations (0.05–0.56 mol L^{-1}).[25] These approaches all involve heterogeneous catalysts and depend on excess of hydrogen peroxide, which may reduce selectivity and feasibility.

Furthermore, other copper-based complexes have been reported as homogeneous catalysts for H_2Q oxidation. For example, bis(dimethylglyoxime) copper(II) and 5,7,7,12,14,14-hexamethyl-1,4,8,11-tetraazacyclotetradeca-4,11-dienatocopper (II)iodide were evaluated as peroxidase mimics in cetyltrimethylammonium bromide (CTAB) micellar solutions. These systems showed strong catalytic activity with H_2O_2, attributed to the active center and favorable micellar environments. However, their dependence on both surfactants and H_2O_2 may limit practical applications.

A heterogeneous microporous metal–organic framework (MOF) $Cu_3(BTC)_2(H_2O)_x$ catalyzed the H_2Q oxidation using

molecular oxygen as the oxidant. This MOF achieved a rate constant (k_{obs}) of 0.168 min^{-1} (0.0028 s^{-1}) at 40 °C. In comparison, the proposed complex **1** demonstrated a significantly higher k_{obs} value of 5.35 s^{-1}, indicating superior catalytic performance.[26]

In the context of developing sensing devices for H_2Q detection, such as optical or electrochemical sensors, the need to avoid external reagents like H_2O_2 is crucial. Importantly, previous Cu(II)-based catalysts were evaluated only for H_2Q oxidation in aqueous media, without assessing selectivity against other phenolic substrates. In contrast, the current study demonstrates the selectivity of complexes **1** and **3**, as evidenced by their catalytic activity toward H_2Q in comparison to *ortho*- and *meta*-substituted phenolic compounds.

One of the most essential functions of catalysts in catalytic oxidation is the activation of oxygen. Based on the results of this work, a probable mechanistic pathway for the oxidation of H_2Q catalyzed by complexes **1** and **3** involves dioxygen being adsorbed and activated by the metal ion active sites, after which it reacts with H_2Q to form Q.[26]

Magnetic properties and theoretical study of 1 and 2

The magnetic behavior of **1** and **2** in the form of $\chi_M T$ *vs.* T plots [χ_M being the direct-current (dc) molar susceptibility per dicopper(II) unit] is shown in Fig. 5 and S11,‡ respectively. At room temperature, $\chi_M T$ is equal to 0.80 (**1**) and 0.81 $cm^3\ mol^{-1}$ K (**2**), values which are close to the expected one for two magnetically isolated copper(II) ions. $\chi_M T$ remains almost constant until 50 K, and it further increases continuously to reach 0.97 (**1**) and 0.98 $cm^3\ mol^{-1}$ K (**2**) at 2.0 K. These features are characteristic of ferromagnetically coupled dicopper(II) systems, such as **1** and **2**. The magnetic data were fitted through the Bleaney–Bowers equation,[27] which is derived from the spin Hamiltonian $\boldsymbol{H} = -J\boldsymbol{S}_{Cu1}\cdot\boldsymbol{S}_{Cu2} + \beta H(g_{Cu1}\boldsymbol{S}_{Cu1} + g_{Cu2}\boldsymbol{S}_{Cu2})$ where J stands for the exchange magnetic coupling parameter and $g_{Cu1} = g_{Cu2} = g$ is the average Landé factor considered isotropic. The theoretical curves are in good agreement with the experimental data and provide the following set of best-fit parameters: g = 2.06 (**1**)/2.08 (**2**) and J = +1.83 (**1**)/+1.72 cm^{-1} (**2**).

The near-identical magnetic coupling observed between **1** and **2** eliminates the possibility of significant magnetic interactions between neighbouring metallacyclophane units in **2** across the diamagnetic sodium(I) cation bridge, suggesting that the extended acriba^{4-} spacer mediates in both compounds the ferromagnetic coupling (F) between two Cu^{II} ions separated by *ca.* 11.5 Å within the dinuclear metallacyclophane unit. DFT calculations on the experimental geometry of **1** align well with these experimental results, corroborating the presence of a moderate ferromagnetic coupling (J = +5.5 cm^{-1}, +5.8 cm^{-1} when using the TZVP basis set for all atoms). These calculations reveal that the non-negligible strength and ferromagnetic nature of this coupling arise from a spin polarization mechanism operating through the π-pathway of the spacer. The specific arrangement of the metal fragment relative to the spacers facilitates the delocalization of Cu^{II} ion's spin density onto the spacer's π-system, resulting in an alternating spin density distribution across the acridine bridge (see Fig. 6). This efficient spin polarization mechanism, which establishes and controls long-range magnetic coupling, is consistent with previous magneto-structural studies on polynuclear metal complexes.[13b,28–31] However, the partial discrepancy between theoretical and experimental magnetic coupling strengths needs to be discussed. Potential structural changes upon cooling the sample must be considered, as the plasticity of the Cu^{II} coordination environment may lead to subtle rearrangements that minimize π–π interactions in the eclipsed conformation of the stacked spacers. Even minor structural distortions can significantly impact the magnetic interaction, as the effectiveness of the spin polarization mechanism—and consequently, the strength of magnetic coupling—relies on the Cu^{II} ion's ability to delocalize its spin density along the spacer's π-pathway. Calculations indicate that in the optimized geome-

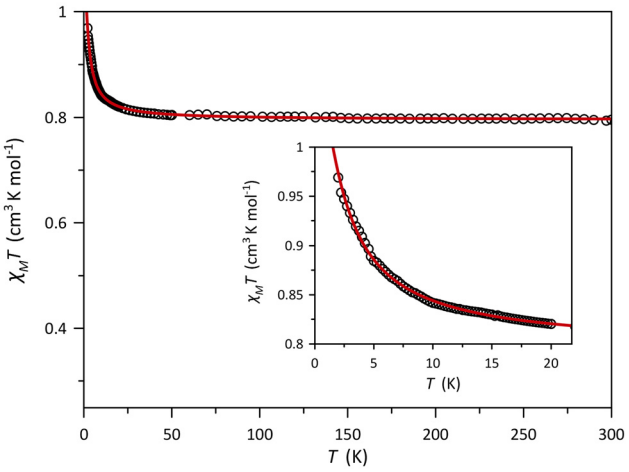

Fig. 5 Thermal dependence of $\chi_M T$ for **1**: (empty circles) experimental; (solid line) best-fit curve through the Bleaney–Bowers equation. The inset shows details of the low-temperature region.

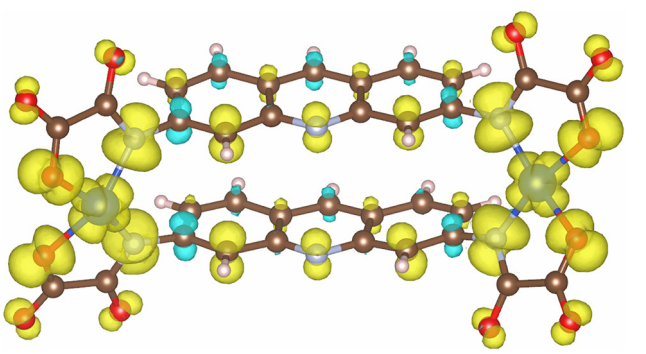

Fig. 6 Spin density distribution in the triplet ground state of the dicopper(II) metallacyclophane unit of **1** (the water molecules were omitted). Yellow and blue colours represent positive and negative isodensity surfaces with a cut-off value of 0.001 e $bohr^{-3}$.

try, the exchange magnetic coupling decreases to +3.4 cm^{-1}, highlighting the sensitivity of magnetic coupling to minimal structural variations, which offers a plausible explanation for the differences observed between theoretical and experimental J values. Nonetheless, the optimized structure appears excessively distorted (see ESI‡), and even in this extreme case, DFT calculations still overestimate the magnetic interaction, which raises concerns about the accuracy of the DFT methods, suggesting that electron delocalization errors—known limitations of many DFT approaches—may contribute to both exaggerated structural distortions and overestimated coupling strengths, a topic that will be further explored.

Introducing a nitrogen atom into the organic spacer is a recognized strategy for modulating ferromagnetic coupling. This effect was previously observed in the complexes $Na_4[Cu_2(mpba)_2]\cdot 10H_2O$ [H_4mpba = *N*,*N*′-1,3-phenylenebis (oxamic acid)] and **3**, where intramolecular ferromagnetic interaction of varying strength occurred through *meta*-substituted phenyl (–Namidate–C–C–C–Namidate–) and pyridyl (–Namidate–C–N–C–Namidate–) skeletons, with J values of +16.8 and +7.9 cm^{-1}, respectively.[13b] These differences were attributed to variations in local spin densities along the organic bridge. Specifically, $Na_4[Cu_2(mpba)_2]\cdot 10H_2O$ exhibited higher spin densities than **3**, leading to enhanced spin polarization and stronger coupling. However, a direct comparison between **1** and **2** is complicated by differences in spacer size. While nitrogen incorporation in the spacer is expected to weaken magnetic coupling, a precise assessment requires a direct comparison with an analogous system lacking nitrogen, which, to our knowledge, is currently unavailable.

Computational modelling of dinuclear systems analogous to **1** and **2** offers valuable insights into the development of magnetic interactions in these compounds. By employing models with perfectly stacked spacers and perpendicularly oriented metal fragments to maximize delocalization along the spacer's π-pathway, we systematically examined the impact of spacer length (N = 1 to 5 phenyl or pyridine rings, Fig. 7) on the singlet–triplet gap (Δ_{S-T}), a proxy for the magnetic coupling constant J in the shorter members of the series.

Despite the substantial separation between these paramagnetic centres (6.57–16.54 Å), our results consistently reveal ferromagnetic interaction between the Cu^{II} ions across all spacer lengths, which aligns with a dominant spin polarization mechanism and an odd exchange pathway within the spacer. The spin polarization effect is more pronounced in the triplet state than in the singlet state, where opposing spin densities on metal ions partially compensate for each other's polarization effects (Fig. S12 and S13‡). Furthermore, Δ_{S-T} is larger with oligoacene than with pyridine-oligoacene spacers (see Fig. 8), which can be attributed to a more significant spin polarization (more pronounced alternating spin) in the oligoacene spacers, as supported by local spin density analysis (Fig. 9).

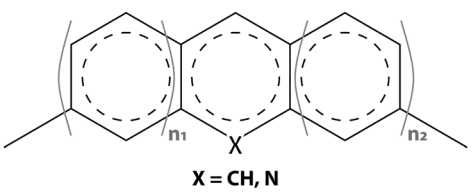

n_1	n_2	N
0	0	1
1	0	2
1	1	3
2	1	4
2	2	5

Fig. 7 Schematic view of the spacer in the studied ideal dinuclear models.

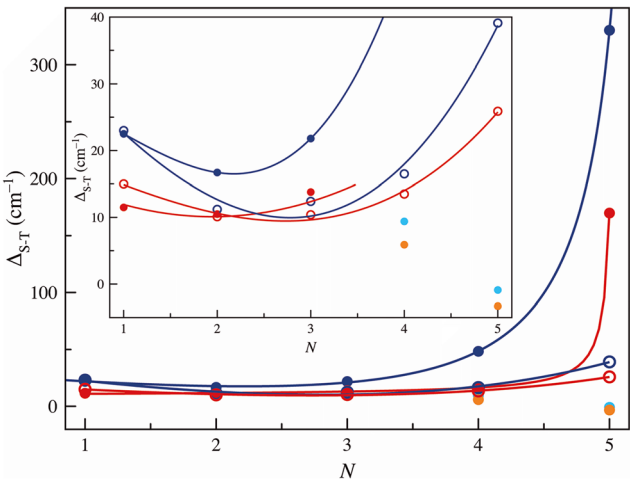

Fig. 8 Spacer size dependence of the Δ_{S-T} triplet-BS singlet energy gap (full circles) for the X = CH (blue) and X = N (red) series (see Fig. 7). The lighter colored points correspond to the most stable configurations for N = 4 and 5, those with a singlet-fission character and a stronger antiferromagnetic coupling between the stacked spacers (see text). The equivalent results found in the optimized geometries are shown as empty circles. Inset shows a magnified view of Δ_{S-T} between −5 and 40 cm^{-1}.

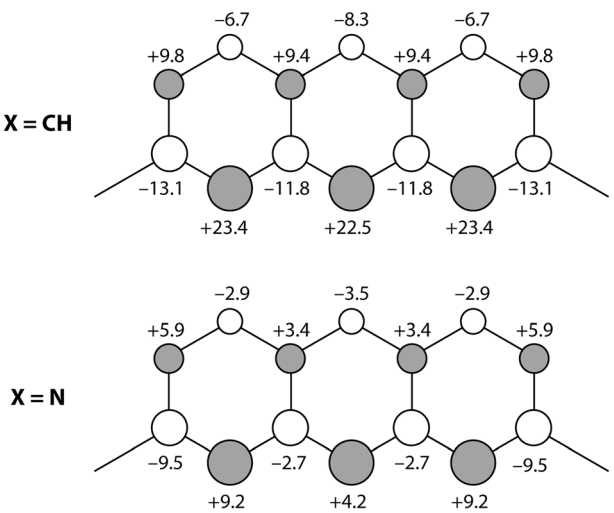

Fig. 9 Schematic representation of the local spin density distribution on the bridging pathways for N = 3 ideal models with oligoacene and pyridine-oligoacene spacers. Full and empty contours denote positive and negative values of the spin density. Calculated atomic densities in me^- are given in parentheses.

In both series, local spin densities increase with N due to excited π states appearing closer to the spacer's ground state, facilitating singlet fission by extending the aromatic system—a phenomenon well-documented in pentacene.[32,33] However, this phenomenon is moderated in the first three members of both series, with only a slight decrease in Δ_{S-T} despite the considerable intermetallic distance (6.57–11.80 Å). Notably, this energy gap exhibits a minimum for the N = 2 model (Fig. 8), indicating that singlet fission becomes non-negligible in the next member of the series. At this point, the spacer begins to acquire partial polyradical character, and Δ_{S-T} can no longer be strictly interpreted as the exchange constant J describing magnetic interaction between the Cu^{II} ions. While we acknowledge this complexity, we will continue to use this terminology for simplicity. The early emergence of this effect in these families may be attributed to the presence of metallic fragments injecting or delocalizing spin density into the spacer's π path and, therefore, acting as a seed for subsequent spin polarization along it.

As N increases beyond 4, the polyradical character of the spacer becomes increasingly evident, leading to the most stable configurations, triplet (T′) and singlet (S′) states, resulting from a strong antiferromagnetic interaction between the spin densities of the stacked spacers with opposing signs (Fig. 10 and S14‡). This behavior that contrasts with our observations in the shorter members of the series arises when this π–π AF become dominant enough to invert the sign of the spin densities between stacked atoms (as shown by the last members of X = CH_2 and N families in Fig. S12 and 13‡ compared to Fig. S14‡), thereby disrupting the typical spin delocalization pathway from the metal centers and altering both the magnitude and sign of the global Δ_{S-T} (Fig. 8).[34] The observed near-degeneracy of the S′ and T′ states ($\Delta_{S'-T'} \approx 0$) can be explained by examining the spin distribution within the C_{spacer}–$N_{oxamate}$ bond. In both states, regions of aligned and opposing spin densities appear in equal measure, yielding similar energy profiles. Consequently, the calculated energies primarily reflect the antiferromagnetic interaction between the spin densities of the stacked spacers ($J_{\pi-\pi}$). Thus, the $J_{\pi-\pi}$ constant for the N = 4 and 5 family members was estimated at −70 and −270 cm^{-1} for X = N, and significantly larger at −270 and −2170 cm^{-1}, for X = CH. This strong interaction is consistent with the pronounced polyradical nature characteristic of singlet fission. Furthermore, the more intense spin polarization in the X = CH family correlates with the enhanced coupling strength. This singlet-fission phenomenon is also observed in nanographene, essentially an isolated sheet of graphite.[35,36] However, unlike in our metallacyclophanes, the sheets in graphite are not eclipsed, allowing for displacement that minimizes intermolecular electronic contacts and magnetic coupling. This structural flexibility helps explain the pronounced distortions sometimes observed in metallocyclophanes, as discussed earlier.

The findings of this study indicate that while event effects were introduced to mitigate delocalization errors—particularly in systems with anionic ligands coordinated to metal ions—the results remain largely consistent without these effects, exhibiting a slight overestimation of the exchange interaction (J), substantial geometric distortions in optimized geometries, and predominant antiferromagnetic (AF) interactions between stacked spacers in the ideal models. Given these observations, functionals that significantly attenuate over delocalization were chosen for further analysis. However, the preferred functionals (rCAM-B3LYP and CAM-QTP) were unavailable in our computational framework,[37–40] necessitating the use of alternative functionals (CAM-B3LYP, M06-HF, and M11),[41–43]

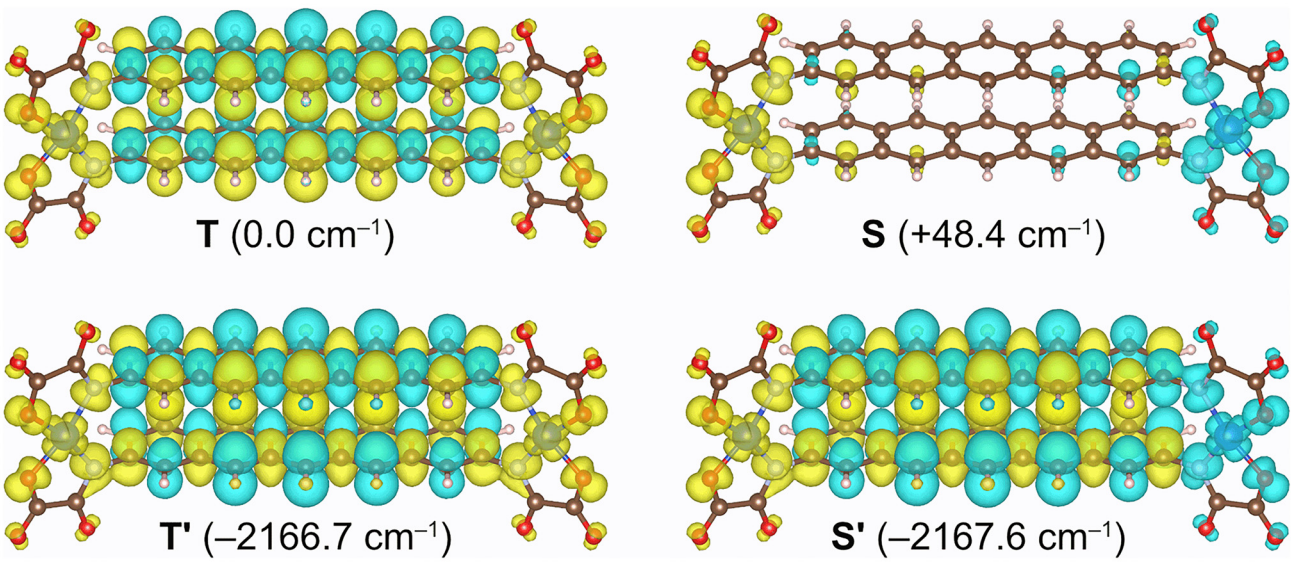

Fig. 10 Calculated spin density maps for T and T′ triplet and S and S′ singlet states of dinuclear copper(II) model featuring oligoacene (X = CH in Fig. 7) spacer of size N = 5 in an idealized geometry (see text). Yellow and blue isodensity surfaces represent positive and negative spin densities with a cut-off value of 0.0018 e $bohr^{-3}$. The numerical values indicate the energy of each state with respect to the triplet T.

which are also recognized for their reliability.[44] Among these alternatives, CAM-B3LYP predicts an even larger J constant (+7.5 cm^{-1}), while M06-HF, known for mitigating delocalization error, suggests a very weak coupling, approaching zero (+0.4 cm^{-1}). In contrast, the M11 functional yields intermediate J values (+4.4 cm^{-1}), aligning more closely with experimental data, particularly when applied to the optimized geometry of the triplet T ground state (+1.7 cm^{-1}). However, all three functionals produce excessively distorted geometries. Given the proven efficiency of the B3LYP functional in evaluating J constants and the consistency of the optimized geometries across all tested density functionals, the apparent improvement in accuracy may be artificial, stemming more from differences in the quality of magnetic coupling evaluation than from a genuine correction of over-delocalization.

Additional optimizations were conducted on a dinuclear nickel(II) complex to investigate the nature of these distortions further. Thus, the Cu^{II} ion in the experimental geometry of **1** (X = N series) was substituted with Ni^{II}, and in a second model (X = CH series), the pyridine nitrogen atom was replaced with a –CH group. Since the Ni^{II} ion in a pseudo-square planar coordination environment is diamagnetic, spin delocalization effects from the metal fragment were eliminated. However, exaggerated molecular distortions persisted in both cases, suggesting that either these distortions are a computational artifact or that the electron density surplus in oxamate anions is excessively delocalized over the spacers. The resulting electronic repulsion between spacers could be responsible for these distortions, warranting further investigation, though this phenomenon does not significantly impact the current discussion.

To assess the influence of spacer electron densities on geometry, optimizations of previously studied models were performed across different series. Given the near invariance of electronic structure in the triplet and singlet states, and considering that singlet fission can be interpreted as a broken-symmetry function of the singlet state, optimizations were conducted on a closed-shell singlet state.[45] The validity of this approximation was confirmed through additional optimizations for the open-shell triplet ground state in representative cases, yielding comparable distortions and supporting the reliability of the closed-shell singlet approximation.

Experimentally, common distortions in metallocyclophanes include spacer bending (α), leading to partial planarity loss; spacer flapping (β); loss of perpendicularity between the spacer and metal fragment planes (γ); slippage between spacers; and partial tetrahedral distortion in the Cu^{II} coordination sphere (Fig. 11 and Table 1). Spacer flapping is unlikely in systems where the substitution pattern maintains major symmetry. Similarly, loss of perpendicularity between spacers and metal fragments, accompanied by slippage, also introduces an additional twist between spacers. These distortions likely separate electron densities of the spacers, particularly in the intermediate region, are evident in optimized geometries – most notably, spacer bending. Starting from a constrained eclipsed initial geometry resulted in moderate distortions compared to those observed experimentally or arising from optimization of the experimental geometry. While these geometries more closely resemble experimental structures, they are not necessarily the most stable; nonetheless, they were chosen based on prior discussions regarding the origins of excessive distortions in this class of compounds.

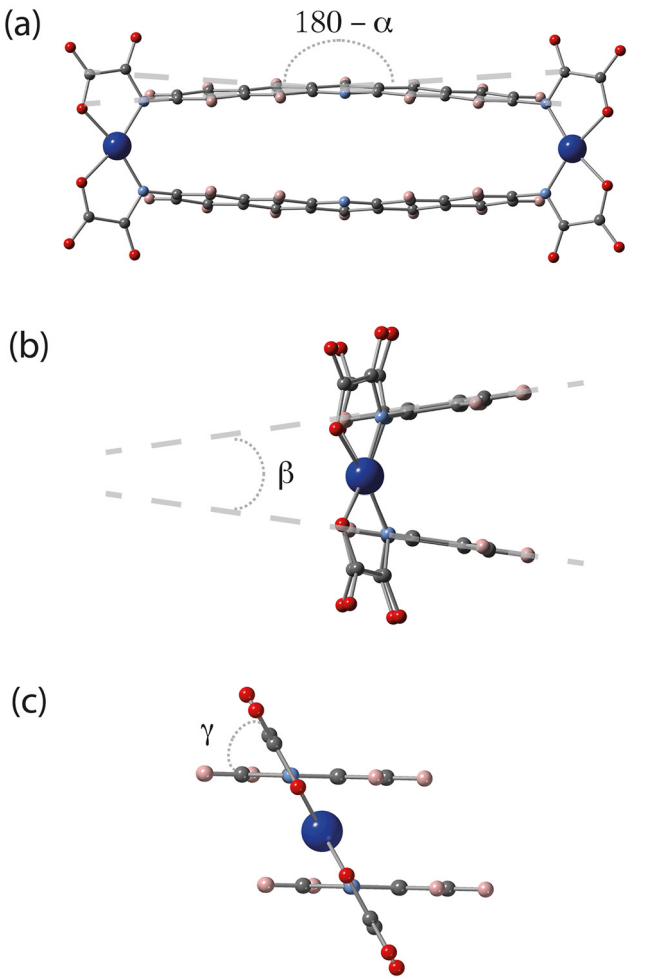

Fig. 11 Schematic representation of the most common distortions in the studied series of dinuclear copper(II) metallocyclophanes: (a) spacer bending [α], (b) spacer flapping [β], and (c) loss of perpendicularity between the spacer and metal fragment planes [γ]. Color code: Cu, dark blue; O, red; N, light blue; C, gray; H, pale pink.

The variation of the singlet–triplet energy gap with spacer size for the two studied families (X = N or CH), when optimized from the eclipsed conformation, is illustrated in Fig. 8. Due to reduced spacer eclipsing, only expected spin configurations (S and T) were observed, indicating an absence of S′ and T′ configurations governed by antiferromagnetic coupling between the spacer spin densities (Fig. S15 and S16‡). The J values followed previously established trends, with the triplet state as the ground state and an initial decrease in J as the spacer extended, reaching a minimum at $N = 2$. These results reinforce the established understanding of electronic interactions in these systems and highlight the role of geometric constraints in modulating electronic and magnetic properties.

Table 1 Values found in series X = CH and N of dinuclear copper(II) and nickel(II) metallocyclophanes from N = 1 to 5 (see Fig. 7) for the selection of geometrical parameters: intramolecular Cu···Cu separation (d_{M-M}), spacer bending (α), spacer flapping (β), and loss of perpendicularity between the spacer and metal fragment planes (γ)

	X = CH				X = N			
N	d_{M-M} (Å)	α (°)	β (°)	γ (°)	d_{M-M} (Å)	α (°)	β (°)	γ (°)
1	6.93	0.5	8.2	86.4	6.57	0.1	13.5	84.4
2	9.33	0.2	21.1	80.9	9.15	2.0	10.3	85.5
3	11.80	1.8	17.3	82.5	11.63	3.2	14.2	83.9
4	14.27	3.1	20.8	80.9	14.09	5.9	12.1	84.8
5	16.74	5.5	15.3	83.3	16.58	5.8	13.4	83.1
Ni, 5	16.77	8.2	13.5	84.2	16.55	6.9	16.3	83.1
1 [a]					11.48	5.2	5.7	69.2

[a] Compound **1**. Average values.

As observed in similar and previously studied amino complexes,[44] intramolecular magnetic communication persists in these systems despite the considerable separation between paramagnetic centers. However, it is less pronounced in the oxamate derivatives. This communication enables their potential use as magnetic wires and in constructing advanced spintronic components. However, oxamate-complex derivatives form metallocyclophane units with strong electronic and magnetic interactions between the stacked spacers, resulting in significant geometric distortions and intense AF coupling. While these factors complicate their study, they also offer opportunities for designing advanced spintronic materials, making metallocyclophanes a promising subject for further academic investigation.

Conclusions

Taking advantage of the π-pathway of the extended spacer, the spin polarization mechanism accounts for the significant ferromagnetic coupling in the dicopper(II) metallacyclophane complexes containing the acridine oxamate-based ligands despite the significant separation between paramagnetic centers (*ca.* 11.5 Å), making them able to act as magnetic wires. The overestimation of magnetic interactions in theoretical models highlights the influence of minor structural distortions but also suggests a potential impact of electron delocalization errors inherent to certain density functionals. The theoretical study also reveals a strong dependence of magnetic interactions on spacer length and composition while confirming the persistence of ferromagnetic coupling over large distances, reinforcing the role of spin polarization in these materials. Notably, introducing nitrogen into the organic spacer modulates ferromagnetic coupling, as evidenced by comparisons with related systems.

Beyond their magnetic properties, these systems also exhibit outstanding reactivity and selectivity in catalysing the oxidation of *para*-substituted isomer hydroquinone (H_2Q), an emerging pollutant, under aerobic conditions. Compared to laccase, which shows a higher affinity toward *ortho*-substituted phenolic compounds, the enhanced selectivity of these two complexes toward the *para*-substituted ones is particularly striking.

Ultimately, these findings open new horizons for developing highly selective platforms for biosensing and biotechnological applications while also underscoring the potential of metallocyclophanes as key building blocks for spintronic devices. Their unique magnetic properties and structural tunability offer promising avenues for designing advanced molecular materials. However, further investigation is required to fully understand the effects of structural distortions and electron delocalization on their magnetic behavior.

Experimental section

General information

All chemicals and solvents were purchased from commercial sources and were used without further purification. $[Na_6Cu_2(mpyba)_2Cl_2(H_2O)_8]\cdot 7H_2O$ (**3**) was synthesized by following a previously reported procedure.[13b] Elemental analysis (C, H, N) was carried out using a ThermoScientific FlashSmart CHNSO Analyzer. ^{1}H NMR for the Et_2H_2(acriba) proligand was conducted by the Microanalytical Service of the Federal University of Goiás. A value of 2 : 1 Na : Cu molar ratio for **1** was determined by electron probe X-ray microanalysis using a Philips XL-30 scanning electron microscopy (SEM) from the Servicio Central de Soporte a la Investigación Experimental (SCSIE) at the University of Valencia.

Synthesis of the Et_2H_2acriba proligand. Triethylamine (0.30 mL, 2.15 mmol) and sodium bicarbonate (0.05 g, 0.59 mol) were added to a solution of 3,6-diaminoacridine hemisulfate salt (0.15 g, 0.58 mmol) with dry pyridine (3.4 mL). Then, ethyloxalyl chloride (0.13 mL, 1.16 mmol) was added to the resulting brown suspension, which was kept under continuous stirring while the whole was maintained in an ice bath to prevent the reaction from heating. The mixture was kept under stirring at room temperature for 90 minutes, and after that time, it was kept in an oil bath under reflux at 80 °C for two hours. The brown solid obtained after adding water was filtered off and washed with an ethanol/water (1 : 1 v/v) solvent mixture to remove any impurity. Yield: 0.220 g; 93%. Anal. calcd for $C_{21}H_{19}N_3O_6$ (**2**): C, 61.61; H, 4.68; N, 10.26. Found: C, 61.59 H, 4.71; N, 10.28%. IR (KBr/cm^{-1}): 3337m [ν(N–H)], 1714s and 1624m [ν(C=O)]. ^{1}H NMR (500 MHz, DMSO-d$_5$): δ 11.16 (s, 1H), 8.92 (s, 1H), 8.61 (s, 2H), 8.10 (d, J = 9.1 Hz, 2H), 7.86 (dd, J = 9.1, 2.1 Hz, 2H), 4.34 (q, J = 7.1 Hz, 2H), 1.33 (t, J = 7.1 Hz, 3H).

Synthesis of $\{Na_4(H_2O)_8[Cu_2(acriba)_2(H_2O)_2]\}_n\cdot 4nH_2O$ (1). Solid NaOH (0.05 g, 1.33 mmol) was poured into an aqueous suspension of Et_2H_2(acriba) (0.13 g, 0.317 mmol). Then, an aqueous solution of $Cu(NO_3)_2\cdot 3H_2O$ (0.07 g, 0.317 mmol) was added dropwise under continuous stirring, and the resulting dark green solution was filtered to discard any particles. Most of the solvent was removed under reduced pressure. A green

precipitate was separated by adding ethanol. It was collected by filtration and washed with ethanol. Yield: 0.239 g, 84%. X-ray quality green needles of **1** were grown after 10 days by slow diffusion of acetonitrile into an aqueous solution of the green solid in a test tube. Anal. calcd for $C_{34}H_{42}Cu_2N_6Na_4O_{26}$ (**1**): C, 34.91; H, 3.62; N, 7.18. Found: C, 34.50; H, 3.55; N, 7.13%. IR (KBr/cm^{-1}): 3405m [ν(O–H)], 1633s and 1594s [ν(C=O)]. UV-Vis (λ_{max}/nm): 563 (on solid) and 646 (in aqueous solution).

Synthesis of $(Bu_4N)_4[Cu_2(acriba)_2]\cdot 5H_2O$ (2). Bu_4NOH 40% in water (0.66 mL, 0.965 mmol) was poured into an aqueous suspension of Et_2H_2acriba (0.10 g, 0.2412 mmol). After complete solubilization, solid $Cu(ClO_4)_2\cdot 6H_2O$ (0.089 g, 0.24 mmol) was added under continuous stirring at room temperature. The resulting green solution was evaporated under reduced pressure until a white precipitate of Bu_4NClO_4 was formed. It was removed by filtration, and the remaining solution was evaporated again under reduced pressure. The green solid obtained was collected and dried under vacuum. Yield: 0.1515 g, 67%. The green needles of **2** suitable for X-ray diffraction were grown by slow evaporation of acetone solutions of the green solid. Anal. calcd for $C_{98}H_{168}Cu_2N_{10}O_{17}$ (**2**): C, 62.42; H, 8.98; N, 7.43. Found: C, 62.35; H, 8.76; N, 7.36%. IR (KBr/cm^{-1}): 3435s [ν(O–H)], 2960s [ν(C–H)], 1639s and 1595s [ν(C=O)]. UV-vis (λ_{max}/nm): 646 (in aqueous solution).

Physical measurements

The infrared spectra of Et_2H_2(acriba), **1** and **2** were recorded on a PerkinElmer Spectrum 400 FT-IR/FT-FIR spectrometer using KBr pellets in the wavenumber range of 4000–400 cm^{-1}. Diffuse reflectance spectra on solid samples of **1** and **2** were measured in a PerkinElmer Lambda WB1050 spectrometer, operating from 250 to 2500 nm spectral range, using a Praying Mantis accessory. UV-Vis absorption spectra of aqueous solutions of **1** and **3** were recorded on a double-beam JASCO V-630 spectrophotometer using quartz cuvettes with 1 cm path length. The temperature was kept at 25 °C by an ETCR-762 (JASCO) water thermostated cell holder with a magnetic stirrer. Magnetic susceptibility measurements on crushed crystals of **1** and **2** were carried out on a Quantum Design SQUID magnetometer operating between 1.9 and 300 K under applied dc magnetic fields of 0.1 T ($T \geq 50$ K) and 500 G ($T < 50$ K). The corrections for the diamagnetism of the constituent atoms were estimated from Pascal's constants[46] as -667×10^{-6} (**1**) and -830×10^{-6} cm^3 mol^{-1} (**2**) [per dicopper(II) unit]. Experimental susceptibilities were also corrected for the temperature-independent paramagnetism [60×10^{-6} cm^3 per mol per copper(II) ion] and the magnetization of the sample holder (a plastic bag).

Kinetic experiments

The reactions were initiated by mixing the solution of the phenolic compound (catechol, resorcinol or hydroquinone) and the catalyst (**1** or **3**) in water at 25 °C under continuous stirring in O_2 or N_2 atmospheres. The oxidation reaction was monitored by acquiring one spectrum every ten minutes for one hour. The concentration of each phenolic compound (75 μmol L^{-1}) was set ten times higher than that of the catalyst (7.5 μmol L^{-1}). Afterwards, the kinetic assay for the hydroquinone oxidation was performed by recording the absorbance at 245 nm *versus* time. The differential method to evaluate the catalytic performance of **1** and **3** was used by acquiring the initial rates directly from the slopes of absorbance–time curves at different values of the initial hydroquinone (H_2Q) concentrations between 5 and 200 μmol L^{-1} while the concentration of catalyst remained fixed at 15 μmol L^{-1}.

Computational details

Density Functional (DF) calculations were carried out on the experimental geometries of the dicopper(II) fragments of **1** and **2** through the Gaussian 09 package using the B3LYP functional,[47] the quadratic convergence approach, and a guess function generated with the fragment of the tool of the same program.[48] Models in ideal geometries or optimized geometries were also studied. Triple-ζ (TZV) and double-ζ (SV) all electron basis sets proposed by Ahlrichs *et al.* were used for the metal and the rest, respectively.[49,50] Several checks were made with other functionals known to reduce the delocalization error typical of methods based on density functional theory (DFT).[51,52] An additional study was also done with TZV basis set adding a p polarization function (TZVP) for all atoms. The states of the magnetic coupling were obtained from the relative energies of the broken symmetry (BS) singlet spin state from the high-spin state with parallel local spin moments. Further details regarding the use of the BS approach to evaluate the magnetic coupling constants can be found in the literature.[53–56]

X-ray crystallography

Room temperature Mo Kα intensity data on single crystals of **1** and **2** were acquired on a Bruker-AXS Kappa Duo diffractometer with an APEX II CCD detector. The crystal structures of both compounds were solved with SHELXS and refined with SHELXL-2018.[57] All non-hydrogen atoms for **1** and **2** were refined with anisotropic parameters except for one water molecule in **1** that was split over two position sites of fixed 60% (O13W, H13A, H13B) and 40% (O14W, H14A, H14B) occupancies, which were found in pilot refinements with a constrained isotropic thermal parameter for the oxygen fractions. Isotropic thermal parameters were used for the hydrogen atoms, which were 20% higher than the U_{eq} values of the bonded atom. In the case of methyl and water hydrogen atoms, this value was 50%. The positions of the hydrogen atoms were calculated respecting both intramolecular and intermolecular geometries, and they were constrained following a riding model (except for those of the water molecules, which were first found from the difference Fourier map and did not oscillate after their fixing). The structure analysis and artwork representations of **1** and **2** were performed on MERCURY[58] and ORTEP-3.[59] Crystallographic data and refinement parameters of **1** and **2** are summarized in Table S1.‡ Selected bond lengths and angles are listed in Tables S2 (**1**)

and S3 (**2**),‡ whereas the hydrogen bonds are given in Tables S4 (**1**) and S5 (**2**).‡ Crystallographic details are available in the ESI‡ in CIF format. CCDC numbers 2083644 (**1**) and 2207096 (**2**).‡

Author contributions

LHGK, MCOES, PVVR, JJSS conducted experiments. LHGK, ACR, SASM, AKSMV, FTM, FL, MJ, RR devised experiments and analyzed the data. JC, LFS, DC directed the research. DC supervised MCOES, PVVR, JJSS, RR. JC supervised RR. LFS supervised PVVR. The manuscript was written through contributions of all authors. All Authors have given their approval to the final version of the manuscript.

Data availability

All data is within the ESI.‡ CCDC 2083644 (**1**) and 2207096 (**2**)‡ contain the supplementary crystallographic data for this paper.

Conflicts of interest

There are no conflicts to declare.

Acknowledgements

This work was funded by the Conselho Nacional de Desenvolvimento Científico e Tecnológico - CNPQ-BRASIL (project no. 305691/2022-8), Fundação de Amparo a Pesquisa de Goiás – FAPEG-BRASIL (projects no. 202310267001369 and 202410267000958) the Spanish MCIN/AEI/10.13039/501100011033 (Projects PID2019-109735GB-I00 and CEX2019-000919-M) and Generalitat Valenciana (AICO/2021/295). M. C. O. E. S. and J. J. S. S. thank CNPQ-BRASIL for undergraduate grants. P. V. V. R. and R. R. (88887.798611/2022-00) thank CAPES-BRASIL for the doctoral and postdoctoral grants.

References

1 C. Rosenzweig and M. H. Sazinsky, *Curr. Opin. Struct. Biol.*, 2006, **16**, 729–735.
2 M. Valles, A. F. Kamaruddin, L. S. Wong and C. F. Blanford, *Catal. Sci. Technol.*, 2020, **10**, 5386–5410.
3 (*a*) Y. Chen and S. Ma, *Dalton Trans.*, 2016, **45**, 9744–9753; (*b*) E. Kuah, S. Toh, J. Yee, Q. Ma and Z. Gao, *Chem. – Eur. J.*, 2016, **22**, 8404–8430.
4 (*a*) J. I. Reyes-De-Corcuera, H. E. Olstad and R. García-Torres, *Annu. Rev. Food Sci. Technol.*, 2018, **9**, 293–322; (*b*) S. Wu, R. Snajdrova, J. C. Moore, K. Baldenius and U. T. Bornscheuer, *Angew. Chem., Int. Ed.*, 2021, **60**, 88–119.
5 G. Janusz, A. Pawlik, U. Świderska-Burek, J. Polak, J. Sulej, A. Jarosz-Wilkołazka and A. Paszczyński, *Int. J. Mol. Sci.*, 2020, **21**, 966.
6 A. Zerva, C. Pentari, A. Termentzi, A. H. P. America, D. Zouraris, S. K. Bhattacharya, A. Karantonis, G. I. Zervakis and E. Topakas, *Biotechnol. Biofuels*, 2021, **14**, 83.
7 B. Bucur, C. Purcarea, S. Andreescu and A. Vasilescu, *Sensors*, 2021, **21**, 3038.
8 (*a*) W.-L. Li and T. Head-Gordon, *ACS Cent. Sci.*, 2021, **7**, 72–80; (*b*) M. Raynal, P. Ballester, A. Vidal-Ferran and P. W. N. M. van Leeuwen, *Chem. Soc. Rev.*, 2014, **43**, 1734–1787.
9 E. Salvadeo, L. Dubois and J.-M. Latour, *Coord. Chem. Rev.*, 2018, **374**, 345–375.
10 (*a*) M. Morimoto, S. M. Bierschenk, K. T. Xia, R. G. Bergman, K. N. Raymond and F. D. Toste, *Nat. Catal.*, 2020, **3**, 969–984; (*b*) M. J. Wiester, P. A. Ulmann and C. A. Mirkin, *Angew. Chem., Int. Ed.*, 2011, **50**, 114–137.
11 Q. Wang, S. H. Brooks, T. Liu and N. C. Tomson, *Chem. Commun.*, 2021, **57**, 2839–2853.
12 (*a*) E. Pardo, R. Ruiz-García, J. Cano, X. Ottenwaelder, R. Lescouëzec, Y. Journaux, F. Lloret and M. Julve, *Dalton Trans.*, 2008, 2780–2805; (*b*) M.-C. Dul, E. Pardo, R. Lescouëzec, Y. Journaux, J. Ferrando-Soria, R. Ruiz-García, J. Cano, M. Julve, F. Lloret, D. Cangussu, C. L. M. Pereira, H. O. Stumpf, J. Pasán and C. Ruiz-Pérez, *Coord. Chem. Rev.*, 2010, **254**, 2281–2296; (*c*) T. Grancha, J. Ferrando-Soria, M. Castellano, M. Julve, J. Pasán, D. Armentano and E. Pardo, *Chem. Commun.*, 2014, **50**, 7569–7585; (*d*) M. Castellano, R. Ruiz-García, J. Cano, J. Ferrando_soria, E. Pardo, F. R. Fortea-Pérez, S.-E. Stiriba, M. Julve and F. Lloret, *Acc. Chem. Res.*, 2015, **48**, 510–520; (*e*) M. Castellano, R. Ruiz-García, J. Cano, J. Ferrando-Soria, E. Pardo, F. R. Fortea-Pérez, S.-E. Stiriba, W. P. Barros, H. O. Stumpf, L. Cañadillas-Delgado, J. Pasán, C. Ruiz-Pérez, G. De Munno, D. Armentano, Y. Journaux, F. Lloret and M. Julve, *Coord. Chem. Rev.*, 2015, **303**, 110–138; (*f*) Y. Journaux, J. Ferrando-Soria, E. Pardo, R. Ruiz-García, M. Julve, F. Lloret, J. Cano, Y. Li, L. Lisnard, P. Yu, H. O. Stumpf and C. L. M. Pereira, *Eur. J. Inorg. Chem.*, 2018, **2018**, 228–247.
13 (*a*) R. Ruiz, J. Faus, F. Lloret, M. Julve and Y. Journaux, *Coord. Chem. Rev.*, 1999, **193–195**, 1069–1117; (*b*) T. S. Fernandes, R. S. Vilela, A. K. Valdo, F. T. Martins, E. García-España, M. Inclán, J. Cano, F. Lloret, M. Julve, H. O. Stumpf and D. Cangussu, *Inorg. Chem.*, 2016, **55**, 2390–2401.
14 (*a*) F. R. Fortea-Pérez, J. Vallejo, M. Julve, F. Lloret, G. De Munno, D. Armentano and E. Pardo, *Inorg. Chem.*, 2013, **52**, 4777–4779; (*b*) J. Vallejo, A. Pascual-Alvarez, J. Cano, I. Castro, M. Julve, F. Lloret, J. Krzystek, G. De Munno, D. Armentano, W. Wernsdorfer, R. Ruiz-García and E. Pardo, *Angew. Chem.*, 2013, **125**, 14075–14079; (*c*) J. W. Maciel, L. H. G. Kalinke, A. K. Valdo, F. T. Martins, R. Rabelo, N. Moliner, J. Cano, M. Julve, F. Lloret and

D. Cangussu, *J. Braz. Chem. Soc.*, 2019, **30**, 2413–2429; (*d*) T. T. da Cunha, V. M. M. Barbosa, W. X. C. Oliveira, C. B. Pinheiro, E. F. Pedroso, W. C. Nunes and C. L. M. Pereira, *Polyhedron*, 2019, **169**, 102–103; (*e*) L. dos S. Mariano, I. M. L. Rosa, N. R. De Campos, A. C. Doriguetto, D. F. Dias, W. D. do Pim, A. K. S. M. Valdo, F. T. Martins, M. A. Ribeiro, E. E. B. De Paula, E. F. Pedroso, H. O. Stumpf, J. Cano, F. Lloret, M. Julve and M. V. Marinho, *Cryst. Growth Des.*, 2020, **20**, 2462–2476; (*f*) T. T. da Cunha, V. M. M. Barbosa, W. X. C. Oliveira, E. F. Pedroso, D. M. A. García, W. C. Nunes and C. L. M. Pereira, *Inorg. Chem.*, 2020, **59**, 12983–12987; (*g*) R. C. A. Vaz, I. O. Esteves, W. X. C. Oliveira, J. Honorato, F. T. Martins, L. F. Marques, G. L. dos Santos, L. O. Freire, L. T. Jesus, E. F. Pedroso, W. C. Nunes, M. Julve and C. L. M. Pereira, *Dalton Trans.*, 2020, **49**, 16106–16124.

15 (*a*) E. Pardo, C. Train, R. Lescouëzec, Y. Journaux, J. Pasán, C. Ruiz-Pérez, F. S. Delgado, R. Ruiz-García, F. Lloret and C. Paulsen, *Chem. Commun.*, 2010, **46**, 2322–2324; (*b*) J. Ferrando-Soria, D. Cangussu, M. Eslava, Y. Journaux, R. Lescouëzec, M. Julve, F. Lloret, J. Pasán, C. Ruiz-Pérez, E. Lhotel, C. Paulsen and E. Pardo, *Chem. – Eur. J.*, 2011, **17**, 12482–12494; (*c*) A. Li, Y. Li, L.-M. Chamoreau, C. Desmarets, L. Lisnard and Y. Journaux, *Eur. J. Inorg. Chem.*, 2020, **2020**, 3311–3319.

16 (*a*) W. X. C. Oliveira, M. M. da Costa, A. P. S. Fontes, C. B. Pinheiro, F. C. S. De Paula, E. H. L. Jaimes, E. F. Pedroso, P. P. de Souza, E. C. Pereira-Maia and C. L. M. Pereira, *Polyhedron*, 2014, **76**, 16–21; (*b*) J. S. González-González, N. E. Magaña-Vergara, E. V. García-Báez, I. I. Padilla-Martínez, J. P. Mojica-Sánchez and F. J. Martínez-Martínez, *Crystals*, 2020, **10**, 1048; (*c*) X. Y. Zhang, L. P. Cheng, Z. J. Zhong, W. Pang and X. Song, *New J. Chem.*, 2022, **46**, 13533–13539; (*d*) V. Kovač, I. Kodrin, K. Radošević, K. Molčanov, B. Adhikari, H.-B. Kraatz and L. Barišić, *Organometallics*, 2022, **41**, 920–936.

17 (*a*) J. Ferrando-Soria, H. Khajavi, P. Serra-Crespo, J. Gascon, F. Kapteijn, M. Julve, F. Lloret, J. Pasán, C. Ruiz-Pérez, Y. Journaux and E. Pardo, *Adv. Mater.*, 2012, **24**, 5625–5629; (*b*) J. Ferrando-Soria, P. Serra-Crespo, M. de Lange, J. Gascon, F. Kapteijn, M. Julve, J. Cano, F. Lloret, J. Pasán, C. Ruiz-Pérez, Y. Journaux and E. Pardo, *J. Am. Chem. Soc.*, 2012, **134**, 15301–15304; (*c*) T. S. Fernandes, W. D. C. Melo, L. H. G. Kalinke, R. Rabelo, A. K. Valdo, C. C. da Silva, F. T. Martins, P. Amorós, F. Lloret, M. Julve and D. Cangussu, *Dalton Trans.*, 2018, **47**, 11539–11553; (*d*) I. F. Silva, I. F. Teixeira, W. P. Barros, C. B. Pinheiro, J. D. Ardisson, G. M. do Nascimento, N. A. Pradie, A. P. C. Teixeira and H. O. Stumpf, *Dalton Trans.*, 2019, **7**, 15225–15232.

18 (*a*) E. Pardo, J. Ferrando-Soria, M.-C. Dul, R. Lescouëzec, Y. Journaux, R. Ruiz-García, J. Cano, M. Julve, F. Lloret, L. Cañadillas-Delgado, J. Pasán and C. Ruiz-Pérez, *Chem. – Eur. J.*, 2010, **16**, 12838–12851; (*b*) E. Pardo, J. Faus, M. Julve, F. Lloret, M. C. Muñoz, J. Cano, X. Ottenwaelder, Y. Journaux, R. Carrasco, G. Blay, I. Fernández and R. Ruiz-García, *J. Am. Chem. Soc.*, 2003, **125**, 10770–10771; (*c*) E. Pardo, R. Carrasco, R. Ruiz-García, M. Julve, F. Lloret, M. C. Muñoz, Y. Journaux, E. Ruiz and J. Cano, *J. Am. Chem. Soc.*, 2008, **130**, 576–585; (*d*) M. Castellano, F. R. Fortea-Pérez, A. Bentama, S.-E. Stiriba, M. Julve, F. Lloret, G. De Munno, D. Armentano, Y. Li, R. Ruiz-García and J. Cano, *Inorg. Chem.*, 2013, **52**, 7645–7657.

19 (*a*) F. R. Fortea-Pérez, I. Schlegel, M. Julve, D. Armentano, G. De Munno and S.-E. Stiriba, *J. Organomet. Chem.*, 2013, **743**, 102; (*b*) F. R. Fortea-Pérez, D. Armentano, M. Julve, G. De Munno and S.-E. Stiriba, *J. Coord. Chem.*, 2014, **67**, 4003–4015; (*c*) F. R. Fortea-Pérez, N. Marino, D. Armentano, G. De Munno, M. Julve and S.-E. Stiriba, *CrystEngComm*, 2014, **16**, 6971–6998; (*d*) F. R. Fortea-Pérez, B. L. Rothenpieler, N. Marino, D. Armentano, G. De Munno, M. Julve and S.-E. Stiriba, *Inorg. Chem. Front.*, 2015, **2**, 1029–1039; (*e*) F. R. Fortea-Pérez, M. L. El Idrissi Moubtassim, D. Armentano, G. De Munno, M. Julve and S.-E. Stiriba, *Inorg. Chem. Front.*, 2018, **5**, 2148–2156; (*f*) M. Tejeda-Serrano, M. Mon, B. Ross, F. Gonell, J. Ferrando-Soria, A. Corma, A. Leyva-Pérez, D. Armentano and E. Pardo, *J. Am. Chem. Soc.*, 2018, **140**, 8827–8832; (*g*) M. Viciano-Chumillas, M. Mon, A. Corma, A. Leyva-Pérez, D. Armentano and E. Pardo, *Acc. Chem. Res.*, 2020, **53**, 520–531.

20 C. Di Giorgio, K. Shimi, G. Boyer, F. Delmas and J.-P. Galy, *Eur. J. Med. Chem.*, 2007, **42**, 1277–1284.

21 V. Addison, T. N. Rao, J. Reedijk, J. Van Rijn and G. C. Verschoor, *J. Chem. Soc., Dalton Trans.*, 1984, 1349–1356.

22 Y. Wu, L.-G. Qiu, W. Wang, Z.-Q. Li, T. Xu, Z.-Y. Wu and X. Jiang, *Transition Met. Chem.*, 2009, **34**, 263–268.

23 M. R. Maurya and S. Sikarwar, *J. Mol. Catal. A: Chem.*, 2007, **263**, 175–185.

24 E. Guibal, T. Vincent, E. Touraud, S. Colombo and A. Ferguson, *J. Appl. Polym. Sci.*, 2006, **100**, 3034–3043.

25 (*a*) I. Owsik and B. Kolarz, *J. Mol. Catal. A: Chem.*, 2002, **178**, 63–71; (*b*) I. A. Owsik and B. N. Kolarz, *Catal. Today*, 2004, **91–92**, 199–204.

26 Y. Wu, L. G. Qiu, W. Wang, *et al.*, *Transition Met. Chem.*, 2009, **34**, 263–268.

27 B. Bleaney and K. D. Bowers, *Proc. R. Soc. A*, 1952, **214**, 451–465.

28 I. Fernandez, R. Ruiz, J. Faus, M. Julve, F. Lloret, J. Cano, X. Ottenwaelder, Y. Journaux and M. C. Muñoz, *Angew. Chem., Int. Ed.*, 2001, **40**, 3039–3042.

29 S. P. Foxon, G. R. Torres, O. Walter, J. Z. Pedersen, H. Toftlund, M. Hüber, K. Falk, W. Haase, J. Cano, F. Lloret, M. Julve and S. Schindler, *Eur. J. Inorg. Chem.*, 2004, 335–343.

30 J. Ferrando-Soria, O. Fabelo, M. Castellano, J. Cano, S. Fordham and H.-C. Zhou, *Chem. Commun.*, 2015, **51**, 13381–13384.

31 D. Cangussu, E. Pardo, M.-C. Dul, R. Lescouezec, P. Herson, Y. Journaux, E. F. Pedroso, C. L. M. Pereira, H. O. Stumpf, M. C. Muñoz, R. Ruiz-García, J. Cano, M. Julve and F. Lloret, *Inorg. Chim. Acta*, 2008, **361**, 3394–3402.
32 M. W. B. Wilson, A. Rao, B. Ehrler and R. H. Friend, *Acc. Chem. Res.*, 2013, **46**, 1330–1338.
33 M. B. Smith and J. Michl, *Chem. Rev.*, 2010, **110**, 6891–6936.
34 H. M. McConnell, *J. Chem. Phys.*, 1963, **39**, 1910.
35 P. M. Greißel, G. M. Beneventi, R. Weiß, A.-S. Wollny, R. K. Dubey, M. Melle-Franco, T. Clark, A. Mateo-Alonso and D. M. Guldi, *J. Am. Chem. Soc.*, 2025, **147**, 11277–11290.
36 W. Zeng and J. Wu, *Chem*, 2021, **7**, 358–386.
37 D. Hait and M. Head-Gordon, *J. Phys. Chem. Lett.*, 2018, **9**, 6280–6288.
38 A. J. Cohen, P. Mori-Sánchez and W. Yang, *J. Chem. Phys.*, 2007, **126**, 191109.
39 P. Verma and R. J. Bartlett, *J. Chem. Phys.*, 2014, **140**, 18A534.
40 Y. Jin and R. J. Bartlett, *J. Chem. Phys.*, 2016, **145**, 034107.
41 T. Yanai, D. P. Tew and N. C. Handy, *Chem. Phys. Lett.*, 2004, **393**, 51–57.
42 Y. Zhao and D. G. Truhlar, *J. Phys. Chem. A*, 2006, **110**, 13126–13130.
43 R. Peverati and D. G. Truhlar, *J. Phys. Chem. Lett.*, 2011, **2**, 2810–2817.
44 D. Hait and M. Head-Gordon, *J. Phys. Chem. Lett.*, 2018, **9**, 6280–6288.
45 J. Cano, F. Lloret and M. Julve, *Dalton Trans.*, 2016, **45**, 16700–16708.
46 A. Earshaw, *An Introduction to Magnetochemistry*, Academic Press, London, U.K., 1968.
47 (*a*) A. D. Becke, *Phys. Rev. A: At., Mol., Opt. Phys.*, 1988, **38**, 3098–3100; (*b*) C. Lee, W. Yang and R. G. Parr, *Phys. Rev. B: Condens. Matter Mater. Phys.*, 1988, **37**, 785–789; (*c*) A. D. Becke, *J. Chem. Phys.*, 1993, **98**, 5648–5652; (*d*) N. R. de Campos, M. A. Ribeiro, W. X. C. Oliveira, D. O. Reis, H. O. Stumpf, A. C. Doriguetto, F. C. Machado, C. B. Pinheiro, F. Lloret, M. Julve, J. Cano and M. V. Marinho, *Dalton Trans.*, 2016, **45**, 172–189.
48 M. J. Frisch, G. W. Trucks, H. B. Schlegel, G. E. Scuseria, M. A. Robb, J. R. Cheeseman, G. Scalmani, V. Barone, B. Mennucci, G. A. Petersson, H. Nakatsuji, M. Caricato, X. Li, H. P. Hratchian, A. F. Izmaylov, J. Bloino, G. Zheng, J. L. Sonnenberg, M. Hada, H. Ehara, K. Toyota, H. Nakai, T. Vreven, J. A. J. Montgomery, J. E. Peralta, F. Ogliaro, M. Bearpark, J. J. Heyd, E. Brothers, K. N. Kudin, V. N. Staroverov, R. Kobayashi, J. Normand, K. Raghavachari, A. Rendell, J. C. Burant, S. S. Iyengar, J. Tomasi, M. Cossi, N. Rega, J. M. Millam, M. Klene, J. E. Knox, J. B. Cross, V. Bakken, C. Adamo, J. Jaramillo, R. Gomperts, R. E. Stratmann, O. Yazyev, A. J. Austin, R. Cammi, C. Pomelli, J. W. Ochterski, R. L. Martin, K. Morokuma, V. G. Zakrzewski, G. A. Voth, P. Salvador, J. J. Dannerberg, S. Dapprich, A. D. Daniels, Ö. Farkas, J. B. Foresman, J. V. Ortiz, J. Cioslowski and D. Fox, *Gaussian 09*, Gaussian, Inc., Wallingford CT, 2009.
49 A. Schäfer, H. Horn and R. Ahlrichs, *J. Chem. Phys.*, 1992, **97**, 2571–2577.
50 A. Schäfer, C. Huber and R. Ahlrichs, *J. Chem. Phys.*, 1994, **100**, 5829–5835.
51 P. Mori-Sánchez, A. J. Cohen and W. Yang, *J. Chem. Phys.*, 2006, **125**, 201102.
52 P. Mori-Sánchez, A. J. Cohen and W. Yang, *Phys. Rev. Lett.*, 2008, **100**, 146401.
53 (*a*) E. Ruiz, P. Alemany, S. Alvarez and J. Cano, *J. Am. Chem. Soc.*, 1997, **119**, 1297–1303; (*b*) E. Ruiz, P. Alemany, S. Alvarez and J. Cano, *Inorg. Chem.*, 1997, **36**, 3683–3688.
54 E. Ruiz, J. Cano, S. Alvarez and P. Alemany, *J. Comput. Chem.*, 1999, **20**, 1391–1400.
55 E. Ruiz, A. Rodríguez-Fortea, J. Cano, S. Alvarez and P. Alemany, *J. Comput. Chem.*, 2003, **24**, 982–989.
56 E. Ruiz, S. Alvarez, J. Cano and V. Polo, *J. Chem. Phys.*, 2005, **123**, 164110.
57 G. M. Sheldrick, *Acta Crystallogr., Sect. C: Struct. Chem.*, 2015, **71**, 3–8.
58 C. F. Macrae, I. J. Bruno, J. A. Chisholm, P. R. Edgington, P. McCabe, E. Pidcock, L. Rodriguez-Monge, R. Taylor, J. Van De Streek and P. A. Wood, *J. Appl. Crystallogr.*, 2008, **41**, 466–470.
59 L. J. Farrugia, *J. Appl. Crystallogr.*, 2012, **45**, 849–854.